Vietnam Journal of Earth Sciences, 48(2), 333−352, https://doi.org/10.15625/2615-9783/24314

Vietnam Journal of Earth Sciences
https://vjs.ac.vn/index.php/jse

On the calculation of vertical derivatives of potential fields for downward continuation and related filters

Saulo Pomponet Oliveira[1], Long Duc Luu[2], Thu-Hang Thi Nguyen[2], Kha Van Tran[3], Luan Thanh Pham[2*]

[1]*Department of Mathematics and Graduate Program in Geology, Federal University of Paraná, Caixa Postal 19096, Curitiba, PR, Brazil*
[2]*University of Science, Vietnam National University, Hanoi, Vietnam*
[3]*Institute of Earth Sciences, VAST, Hanoi, Vietnam*

Received 17 December 2025; Received in revised form 26 February 2026; Accepted 09 March 2026

ABSTRACT

Methods for enhancing and estimating parameters of potential fields from gravimetric and magnetometric surveys typically utilize the vertical derivatives (VDR) of the potential field. These derivatives amplify the high-frequency content of the field, which can be caused by shallow bodies or survey noise. Regularization methods generate approximations of derivatives that must reconcile two objectives: reducing the effect of high-frequency amplification and providing an accurate approximation. Achieving this balance is crucial for methods that require vertical derivatives of successive order, such as Taylor-series implementations of downward continuation and the enhanced horizontal derivative (EHD) filter. This paper evaluates the performance of several vertical-derivative methods for downward continuation and EHD filters using both noise-free and noisy synthetic data. In addition, gravity data over the SW Sub-basin are considered, and the findings are compared with seismic data. Our results show that the β-VDR method provides more accurate and stable derivatives under noisy conditions.

Keywords: Vertical derivative, potential field data, data enhancement, SW Sub-basin.

1. Introduction

The utility of the vertical derivative (VDR) for interpreting potential field data has long been recognized in the literature (Evjen, 1936; Peters, 1949; Henderson and Zietz, 1949). In comparison with the original field, the VDR shows more clearly the separation between neighboring anomalies and suppresses regional effects (Evjen, 1936). Besides its utility as a qualitative method, it can provide depth estimates for sources with simple geometry (e.g., Peters, 1949).

The VDR is often combined with other spatial derivatives, or with higher-order vertical derivatives in the design of both qualitative and semiquantitative methods. One of the earliest ones was downward continuation (Peters, 1949; Dean, 1958). Some of the classical approaches that are still used in practice are the analytic signal amplitude (Nabighian, 1972), Euler deconvolution (Thompson, 1982; Reid et al., 1990; Melo et al., 2020; Pham et al., 2024), tilt angle (Miller and Singh, 1994), and some edge detectors (Ai et al., 2024, 2025; Alvandi et al., 2024, 2025). Currently, high-order

*Corresponding author, Email: luanpt@hus.edu.vn

derivatives are commonly used in mapping geological structures (Altınoğlu et al., 2024; Narayan et al., 2016, 2021, 2024; Sahoo et al., 2022a, b; Aprina et al., 2024; Pham et al., 2025; Saada et al., 2025; Eldosouky et al., 2025; Öksüm et al., 2025).

The instability of vertical derivative calculations has long been recognized. The classical frequency-domain calculation (Bhattacharyya, 1965; Blakely, 1996) is simple and accurate, but it amplifies high-frequency content and is thus highly susceptible to noise. The earliest recommendations to mitigate this issue were to increase the grid spacing (Henderson, 1960) and to perform low-pass filtering before processing (Naidu, 1966; Clarke, 1969; Reilly, 1969).

Later on, several alternatives to data filtering have been proposed in the literature. Nabighian (1984) computed the vertical derivative from the Hilbert transform of the horizontal derivatives (see also Roy, 2013; Luo et al., 2025). Florio et al. (2006) proposed the classical backward finite-difference (FD) formula based on upward continuation for the correct calculation of vertical derivatives of non-harmonic fields. Still, this formula is more stable due to the upward continuation operator (Tatchum et al., 2011). Finite difference formulas of higher order have been derived to increase accuracy while retaining stability (Tran and Nguyen, 2020; Oliveira and Pham, 2022; Pham, 2025a, b). Fedi and Florio (2001) proposed the integrated second vertical derivative (ISVD) method, which computes the vertical integral of the field and then the second vertical derivative in the spatial domain. Pašteka et al. (2009) formulated the VDR calculation under the Tikhonov regularization formalism. Some variations of this formulation and strategies for choosing the regularization parameter have been proposed (Melo et al., 2023; Oliveira et al., 2024; Karcol and Pašteka, 2025). The regularized vertical derivative methods are often considered in the context of calculating vertical derivatives of successive order, in particular for implementing the enhanced horizontal derivative (Fedi and Florio, 2001; Fedi and Florio, 2002), the multiscale derivative analysis (Fedi, 2002; Cella et al., 2009), and the downward continuation (Zhang et al., 2013; Gang and Lin, 2018; Tran and Nguyen, 2020; Pham 2025a).

In this work, we review the accuracy and stability of some VDR methods, such as the standard approach in the frequency domain (Blakely, 1996), ISVD (Fedi and Florio, 2001), FD (Florio et al., 2006), T-N (Tran and Nguyen, 2020), and β-VDR (Oliveira and Pham, 2022; Pham, 2025a) methods. These methods are tested on both noise-free and noisy synthetic data, and are then applied to the enhanced horizontal derivative (EHD) and downward continuation. Finally, we apply the best method to the gravity data over the SW Sub-basin to enhance the data resolution and structural boundaries in this study area.

2. Methods

2.1. Frequency domain method

The standard frequency domain calculation is the most popular method for computing the *n*th-order vertical derivative of magnetic and gravity data. The expression of this method is as follows (Blakely, 1996):

$$f^n = F^{-1}\left[k^n F[f]\right], \qquad (1)$$

where F and F^{-1} are the Fourier and inverse Fourier transforms, and k is the wavenumber.

2.2. ISVD method

The ISVD method (Fedi and Florio, 2001) is based on the Laplace equation to compute vertical derivatives. By using this method, the first derivative is given by the following equation:

$$f' = \frac{\partial f}{\partial z} = \frac{\partial^2 U}{\partial z^2} = -\frac{\partial^2 U}{\partial x^2} - \frac{\partial^2 U}{\partial y^2}, \qquad (2)$$

where U is the vertical integral that is computed as:

$$U = F^{-1}\left[\frac{1}{|k|}F[f]\right], \quad (3)$$

The second vertical derivative is computed through the second horizontal derivatives,

$$f'' = \frac{\partial^2 f}{\partial z^2} = -\frac{\partial^2 f}{\partial x^2} - \frac{\partial^2 f}{\partial y^2}, \quad (4)$$

while higher order derivatives are obtained in the same way, e.g.,

$$f''' = \frac{\partial^3 f}{\partial z^3} = -\frac{\partial^2 f'}{\partial x^2} - \frac{\partial^2 f'}{\partial y^2}. \quad (5)$$

2.3. FD method

Florio et al. (2006) used the FD method to compute the first vertical derivative from the observation and upward continuation fields:

$$f' = \frac{f - f_{\Delta h}}{\Delta h}. \quad (6)$$

We followed the recommendation of Tran and Nguyen (2020) for high-noise data, setting Δh equal to twice the grid spacing.

2.5. β-VDR method

Oliveira and Pham (2022) proposed the β-VDR approach, which is based on a finite-difference formula applied to upward-continued fields to obtain a stable first-order vertical derivative of the field. Their approach is defined as:

$$f' = \frac{p_1 f_{h_1} + p_2 f_{h_2} + p_3 f_{h_3} + p_4 f_{h_4} + p_5 f_{h_5}}{\Delta h}, \quad (9)$$

where the coefficients p_1, ..., p_5 are:

$$\begin{cases} p_1 = (2\beta^3 + 15\beta^2 + 35\beta + 25)/12, \\ p_2 = (-8\beta^3 - 54\beta^2 - 104\beta - 48)/12, \\ p_3 = (12\beta^3 + 72\beta^2 + 114\beta + 36)/12, \\ p_4 = (-8\beta^3 - 42\beta^2 - 56\beta - 16)/12, \\ p_5 = (2\beta^3 + 9\beta^2 + 11\beta + 3)/12, \end{cases} \quad (10)$$

and f_{h_i} denotes the anomaly at height $h_i = \beta\Delta h + (i-1)\Delta h$, where Δh is smaller than the grid spacing, and β is a stabilizing parameter. In this study, we used $\Delta h = 1/10$ of the grid spacing and $\beta = 35$ (Pham, 2025a).

The β-VDR approach can be generalized for the *n*th order vertical derivative as the following equation (Pham, 2025a):

This method can be generalized for the *n*th order vertical derivative as follows:

$$f^n = \frac{f^{n-1} - f^{n-1}_{\Delta h}}{\Delta h}. \quad (7)$$

In our experiment, we have chosen Δh to be one-tenth of the grid spacing, as suggested by Florio et al. (2006).

2.4. Tran-Nguyen (T-N) method

Tran and Nguyen (2020) introduced a new approach for calculating vertical derivatives of the potential field using the observation field and its upward continuation at equally spaced heights $f_{\Delta h}$, $f_{2\Delta h}$,…, $f_{\mathrm{n}\Delta h}$. This approach is based on the Taylor series expansion and determines vertical derivatives by solving the following system of equations for f^1, f^2, ..., and f^{n}:

$$\begin{aligned} f_{\Delta h} &= f - \Delta h\, f^1 + \frac{(-\Delta h)^2}{2!}f^2 + \cdots + \frac{(-\Delta h)^n}{n!}f^n \\ f_{2\Delta h} &= f - 2\Delta h\, f^1 + \frac{(-2\Delta h)^2}{2!}f^2 + \cdots + \frac{(-2\Delta h)^n}{n!}f^n \\ &\vdots \\ f_{\mathrm{n}\Delta h} &= f - n\Delta h\, f^1 + \frac{(-n\Delta h)^2}{2!}f^2 + \cdots + \frac{(-n\Delta h)^n}{n!}f^n. \end{aligned} \quad (8)$$

$$f^n = \frac{p_1 f_{h_1}^{n-1} + p_2 f_{h_2}^{n-1} + p_3 f_{h_3}^{n-1} + p_4 f_{h_4}^{n-1} + p_5 f_{h_5}^{n-1}}{\Delta h}. \quad (11)$$

2.6. Applications to edge detection and downward continuation

Derivatives obtained from the methods are compared by considering the enhanced horizontal derivative (EHD) detector that includes derivatives in its equation (Fedi and Florio, 2001), i.e.,

$$EHD = \sqrt{\left(\frac{\partial \psi}{\partial x}\right)^2 + \left(\frac{\partial \psi}{\partial y}\right)^2}, \quad (12)$$

where ψ is given by:

$$\psi = \sum_{i=i_0}^{n} w_i f^i, \quad (13)$$

and w_i is a set of weights. Here, the EHD was computed using unit weights with n = 3 and either $i_0 = 0$ or $i_0 = 1$ depending on the data. In fact, Fedi and Florio (2001) suggested dropping the lowest-order term to improve the results possibly.

Derivatives are also used for computing the downward continuation at a depth z using the Taylor series:

$$f_{DC} = f + zf' + \frac{z^2}{2!} f'' + \cdots + \frac{z^m}{m!} f^m. \quad (14)$$

The truncation order m controls the balance between accuracy and stability in the downward continuation. Larger values improve the approximation but increase sensitivity to noise due to contributions from higher-order derivatives, whereas smaller values produce smoother but less accurate results. In this work, we used m = 8 to compute the downward continuation as suggested by Tran and Nguyen (2020). The EHD and downward continuation filters are related in the sense that Eq. (14) can be written in the same form as in Eq. (13) with $w_i = \frac{z^i}{i!}$. This motivates considering these filters in the same study.

3. Model studies

3.1. Spherical model

To test the precision and stability of the VDR methods, we used the spherical model (Fig. 1a) with a density contrast of 0.5 g/cm^3, a radius of 20 km, and is located at (x_0, y_0, z_0) = (50 km, 50 km, 30 km). The noise-free and noisy gravity anomaly (Figs. 1b and 1c) obtained from the spherical body are shown in Figs. 1b and 1c, respectively. To estimate the stability of the VDR techniques, a small amount of Gaussian noise with an amplitude of 0.05% of the maximum anomaly was added to the noise-free data (Fig. 1c). For conciseness, we present in Figs. 2-4 the profiles of the derivative maps along a diagonal line, as shown in Fig. 1.

Figs. 2a, 2c, 2e, 2g, and 2i present the first derivatives obtained from applying the standard frequency, ISVD, FD, T-N, and β-VDR methods to the noise-free gravity anomaly in Fig. 1b, respectively. Comparing the theoretical derivative (the dashed line) and calculated derivatives (Figs. 2a, 2c, 2e, 2g, and 2i) shows that all methods are effective in computing the first vertical derivative of the noise-free data. Figs. 2b, 2d, 2f, 2h, and 2j depict the first vertical derivatives of the noisy gravity anomaly in Fig. 1c obtained from the standard frequency, ISVD, FD, T-N, and β-VDR methods, respectively. One can see that these derivatives closely match the theoretical derivative (the dashed line). However, the calculations using the standard frequency (Fig. 2b) and FD (Fig. 2f) methods have produced more noise than other methods. The ISVD (Fig. 2d), T-N (Fig. 2h), and β-VDR (Fig. 2j) methods reduce noise, with the lowest noise level observed in the β-VDR profile.

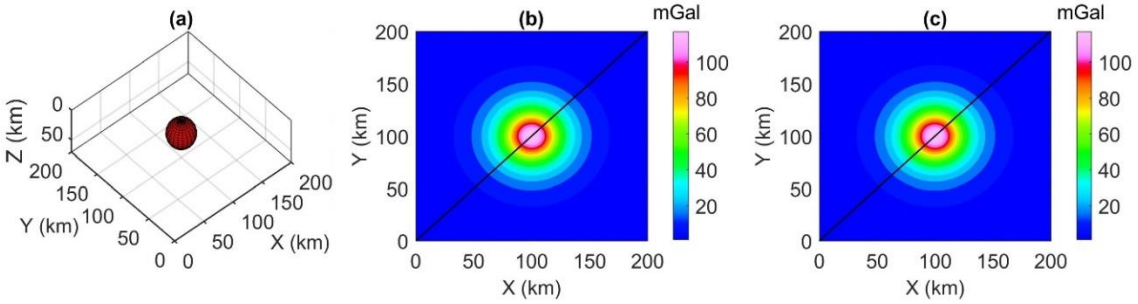

Figure 1. (a) Spherical body, (b) Noise-free gravity anomaly, (c) Noisy gravity anomaly. The black line shows the model's profile.

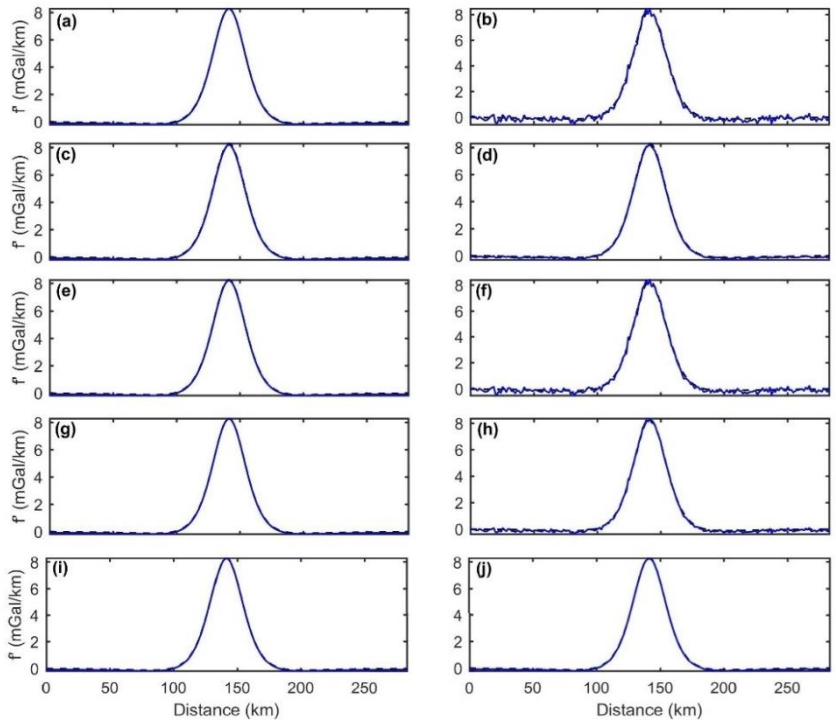

Figure 2. First vertical derivatives of the noise-free data along the profile in Fig. 1: (a) Frequency domain derivative, (c) ISVD derivative, (e) FD derivative, (g) T-N derivative, (i) β-VDR derivative; First vertical derivatives of the noisy data along the profile in Fig. 1: (b) Frequency domain derivative, (d) ISVD derivative, (f) FD derivative, (h) T-N derivative, (j) β-VDR derivative. The dashed lines show the theoretical derivatives

Figs. 3a, 3c, 3e, 3g, and 3i illustrate the second vertical derivatives of the noise-free anomaly computed by using the standard frequency, ISVD, FD, T-N, and β-VDR methods, respectively. The ISVD, FD, T-N, and β-VDR results match very well with the true derivative (the dashed line), while the standard frequency method produces high-frequency modes of small amplitude but visible. Approximations of the second vertical derivative of the noisy anomaly are presented in Figs. 3b, 3d, 3f, 3h, and 3j. In this case, the approximation from the β-VDR method remains stable and closely matches the

theoretical derivative, whereas other approximations are noisy, especially the standard frequency and FD results.

The standard frequency, ISVD, FD, T-N, and β-VDR methods were also used to compute the third derivative of the noise-free anomaly. The standard frequency, ISVD, FD, T-N, and β-VDR derivatives are depicted in Figs. 4a, 4c, 4e, 4g, and 4i, respectively. As can be seen in Figs. 4a and 4e: the standard frequency and FD derivatives are noisy, especially in the frequency domain. The ISVD, T-N, and β-VDR methods yield better solutions for the third derivative of the noise-free anomaly, which closely match the theoretical derivative. Third vertical derivative calculations of the noisy data using the standard frequency, ISVD, FD, T-N, and β-VDR methods are illustrated in Figs. 4b, 4d, 4f, 4h, and 4j, respectively. The noise level from the standard frequency and FD methods is the highest among all approaches. The ISVD and T-N have lower amplitudes than the standard frequency and FD results, but their results are unstable. The β-VDR method still has the lowest noise and shows a clear anomaly in the central region.

Overall, the β-VDR method is more stable and provides more accurate derivatives than other methods. The root mean square (RMS) errors of derivatives computed by the β-VDR method are smaller than those obtained from other methods in all cases (Table 1).

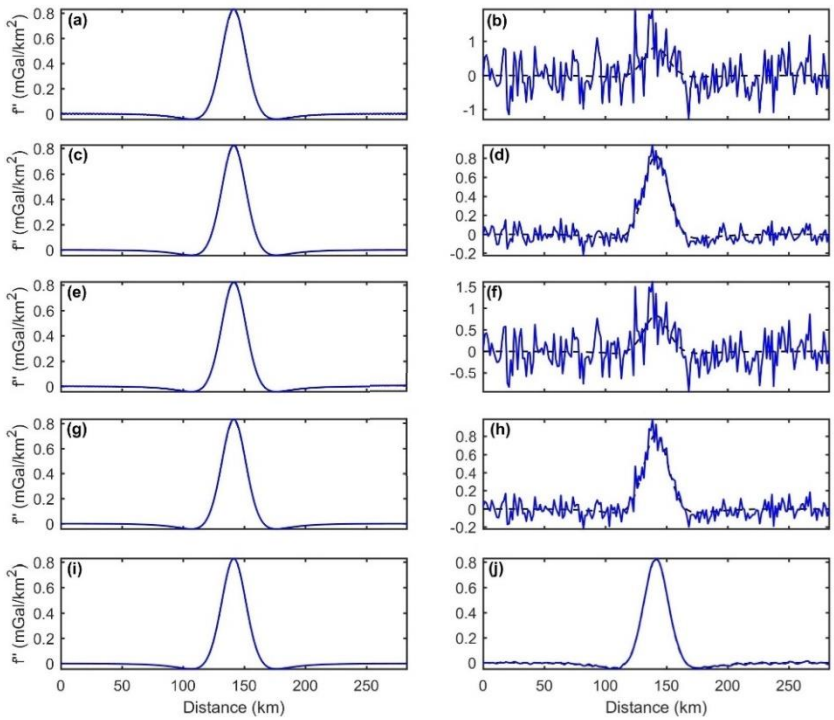

Figure 3. Second vertical derivatives of the noise-free data along the profile in Fig. 1: (a) Frequency domain derivative, (c) ISVD derivative, (e) FD derivative, (g) T-N derivative, (i) β-VDR derivative; Second vertical derivatives of the noisy data along the profile in Fig. 1: (b) Frequency domain derivative, (d) ISVD derivative, (f) FD derivative, (h) T-N derivative, (j) β-VDR derivative. The dashed lines show the theoretical derivatives

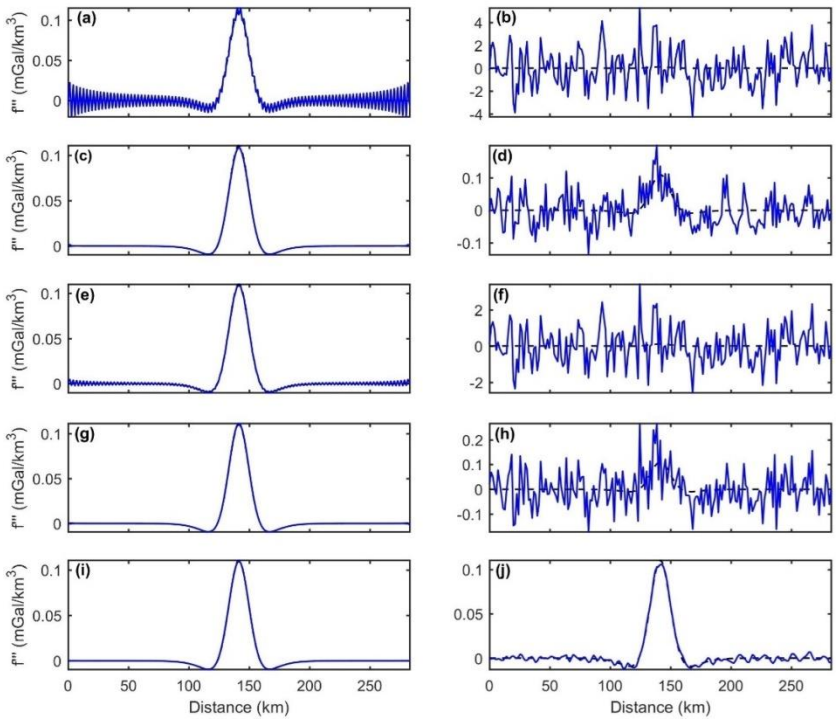

Figure 4. Third vertical derivatives of the noise-free data along the profile in Fig. 1: (a) Frequency domain derivative, (c) ISVD derivative, (e) FD derivative, (g) T-N derivative, (i) β-VDR derivative; Third vertical derivatives of the noisy data along the profile in Fig. 1: (b) Frequency domain derivative, (d) ISVD derivative, (f) FD derivative, (h) T-N derivative, (j) β-VDR derivative. The dashed lines show the theoretical derivatives

Table 1. RMS errors of derivatives obtained from different methods for the spherical model

	Frequency domain	**ISVD**	**FD**	**T-N**	**β-VDR**
First-order derivative (mGal/km)	0.1761	0.0738	0.1554	0.1003	0.0591
Second-order derivative (mGal/km^2)	0.4980	0.0677	0.3647	0.0835	0.0053
Third-order derivative (mGal/km^3)	1.6296	0.0458	0.9951	0.0703	0.0025

3.2. Prismatic model

In this section, we used a prismatic model (Fig. 5a) consisting of three sources, A, B, and C, with their tops located at depths of 11 km, 13 km, and 15 km, respectively, to estimate the effectiveness of using derivatives for edge detection and downward continuation. The prisms A, B, and C have dimensions of 40 × 40 × 3 km^3, 50 × 50 × 7 km^3, and 20 × 20 × 5 km^3, with densities of 0.14 g/cm^3, 0.1 g/cm^3, and 0.05 g/cm^3, respectively. Fig. 5b depicts the gravity anomaly caused by the prisms. In this example, we added Gaussian noise with an amplitude of 0.05% of the maximum anomaly to the noise-free data (Fig. 5c).

Fig. 6 demonstrates the performance of five approaches in computing the first, second, and third vertical derivatives from noisy gravity data. The standard frequency method (Figs. 6a–6c) produces recognizable anomaly patterns in the first derivative but suffers from strong noise amplification in the higher order derivatives. The ISVD method (Figs. 6d–6f) effectively suppresses noise when computing the first derivative, although

the noise is amplified in the second and third derivatives. The FD results (Figs. 6g–6i) retain the main anomaly shapes in the first derivative, but still show noticeable noise contamination at higher derivative orders. The T-N method (Figs. 6j–6l) improves stability and yields cleaner derivative fields than the standard and FD approaches, yet noise remains elevated in higher-order derivatives. In contrast, the β-VDR method (Figs. 6m–6o) presents the most stable and coherent result, preserving anomaly geometry while significantly reducing noise amplification across all derivative orders. The β-VDR derivatives are very similar to the theoretical first-, second-, and third-order derivatives shown in Figs. 5d-5f. In this example, the RMS errors of derivatives computed by the β-VDR method are also smaller than those obtained from other methods (Table 2). Overall, the comparison highlights the superior robustness of the β-VDR technique in calculating high-order derivatives from noisy data.

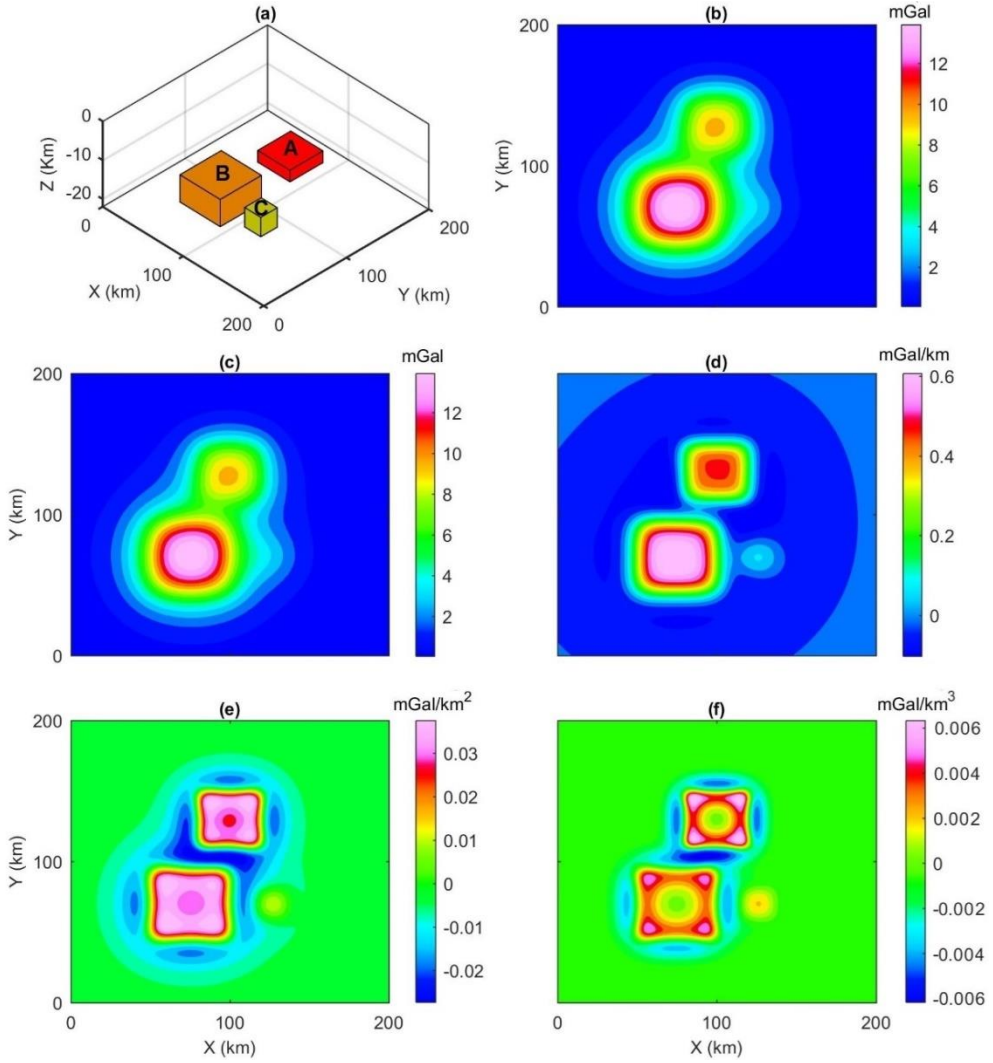

Figure 5. (a) Prismatic bodies, (b) Noise-free gravity anomaly, (c) Noisy gravity anomaly, (d) Theoretical first derivative, (e) Theoretical second derivative, (f) Theoretical third derivative

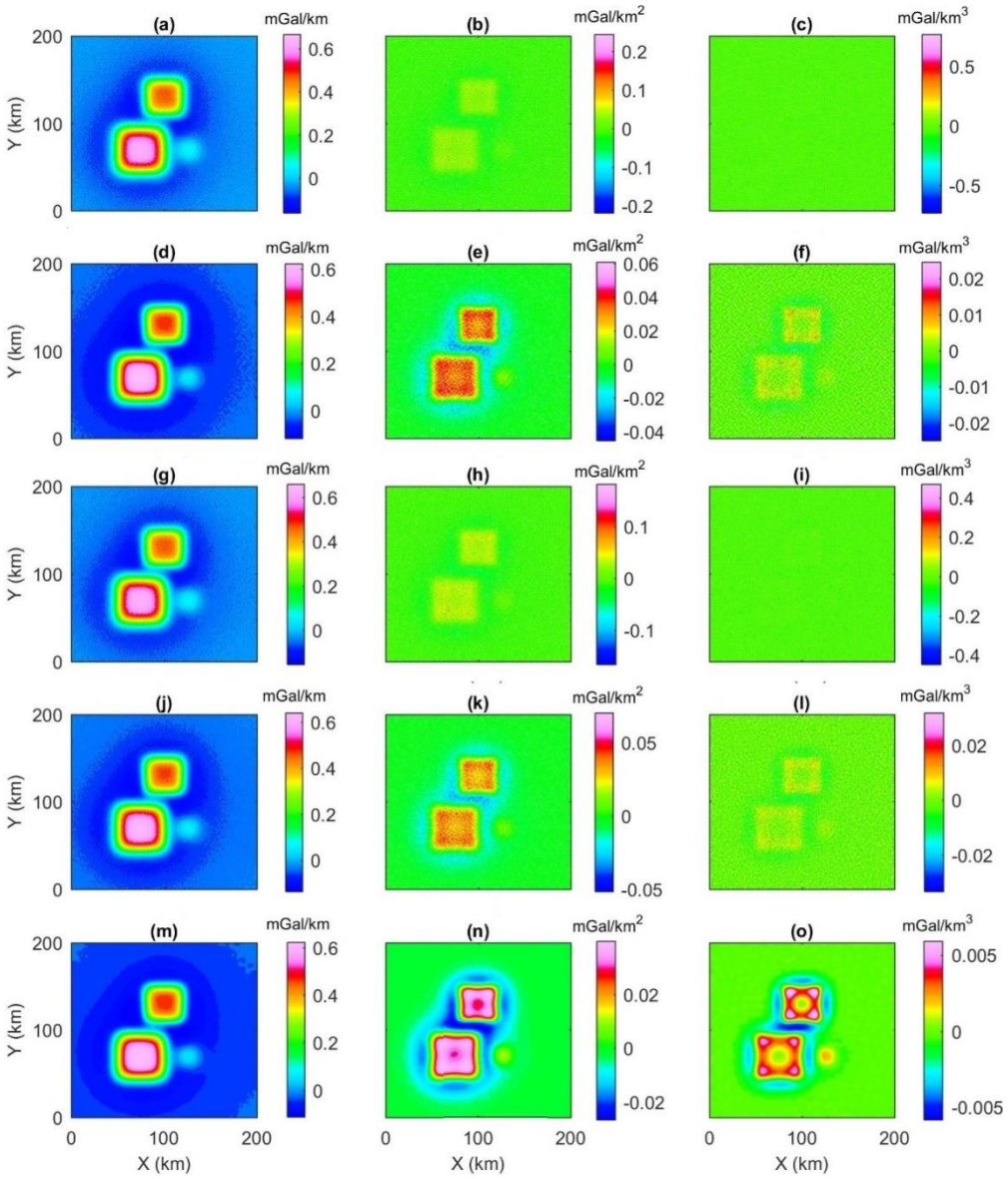

Figure 6. First, second, and third vertical derivatives of the noisy anomaly computed by the standard frequency method (a-c), ISVD method (d-f), FD method (g-i), T-N method (j-l), and β-VDR method (m-o)

Table 2. RMS errors of derivatives obtained from different methods for the prismatic model

	Frequency domain	**ISVD**	**FD**	**T-N**	**β-VDR**
First-order derivative (mGal/km)	0.0213	0.0109	0.0191	0.0136	0.0101
Second-order derivative (mGal/km^2)	0.0571	0.0082	0.0418	0.0097	0.0007
Third-order derivative (mGal/km^3)	0.1885	0.0057	0.1147	0.0081	0.0003

The EHD outputs for noisy data with i ranging from 1 to 3 in Eq. (13), calculated using derivatives obtained from the standard frequency, ISVD, FD, T-N, and β-VDR methods, are shown in Figs. 7b-7f. The EHD maps derived from frequency and FD

derivatives do not show any edges of the sources. The EHD outputs using ISVD and FD derivatives can outline the edges of bodies A and B, but they are faint. In addition, the noise was significantly amplified in these maps. The EHD amplitude obtained from β-VDR derivatives matches well with the theoretical value in Fig. 7a. One can see that the EHD of β-VDR derivatives can delineate the edges of the prisms. As the EHD is an amplitude-based filter, the edges of the deepest source C are blurred.

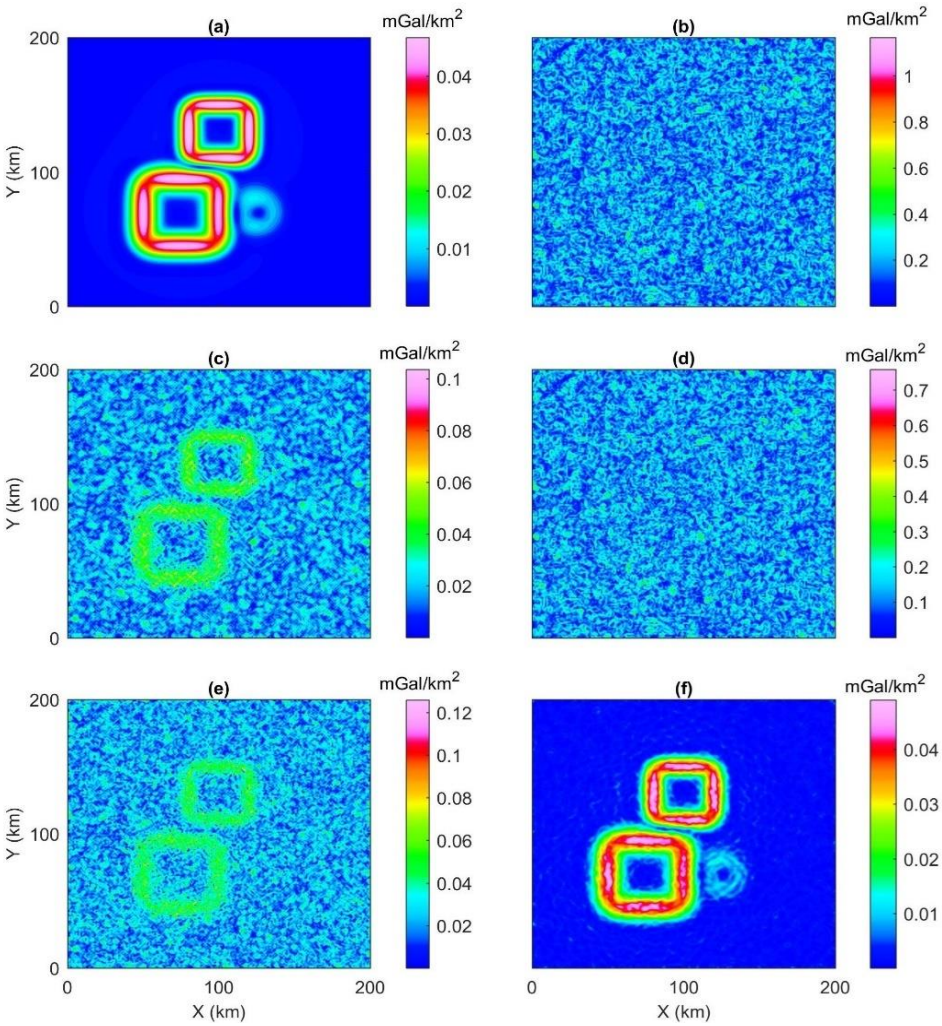

Figure 7. (a) Theoretical EHD and EHD of noisy data calculated by using domain derivatives (b), ISVD derivatives (c), FD derivatives (d), T-N derivatives (e), and β-VDR derivatives (f)

Derivatives from five approaches are also used to compute the downward continuation at depths of 5 and 10 km. Figure 8a shows the theoretical downward continued field at 5 km, while Figs. 8b-8f are 5 km downward-continued fields obtained using frequency, ISVD, FD, T-N, and β-VDR derivatives. One can see that the frequency and FD downward continuation fields are very noisy and do not show any signals from the sources. The ISVD downward continuation can enhance the bodies A and B, but it yields higher amplitudes than those in the theoretical downward continuation map. The T-N and

β-VDR downward continuations are very stable and in good agreement with the theoretical field.

At a continuation depth of 10 km, the theoretical anomaly (Fig. 9a) enhances information of all prisms. However, when using frequency, ISVD, and FD derivatives, the noise is quickly amplified, masking the effective information in the downward-continued anomalies (Figs. 9b-9d). In this case, the T-N and β-VDR downward continuations (Figs. 9e and 9f) are more stable than other methods. These methods effectively suppress noise and reconstruct a field visually close to the theoretical anomaly, preserving anomaly shapes with minimal distortion. The T-N method yields lower noise than the β-VDR downward continuation. However, it is particularly noteworthy that the chosen parameter β is a key parameter to β-VDR, which will be discussed in the following paragraph.

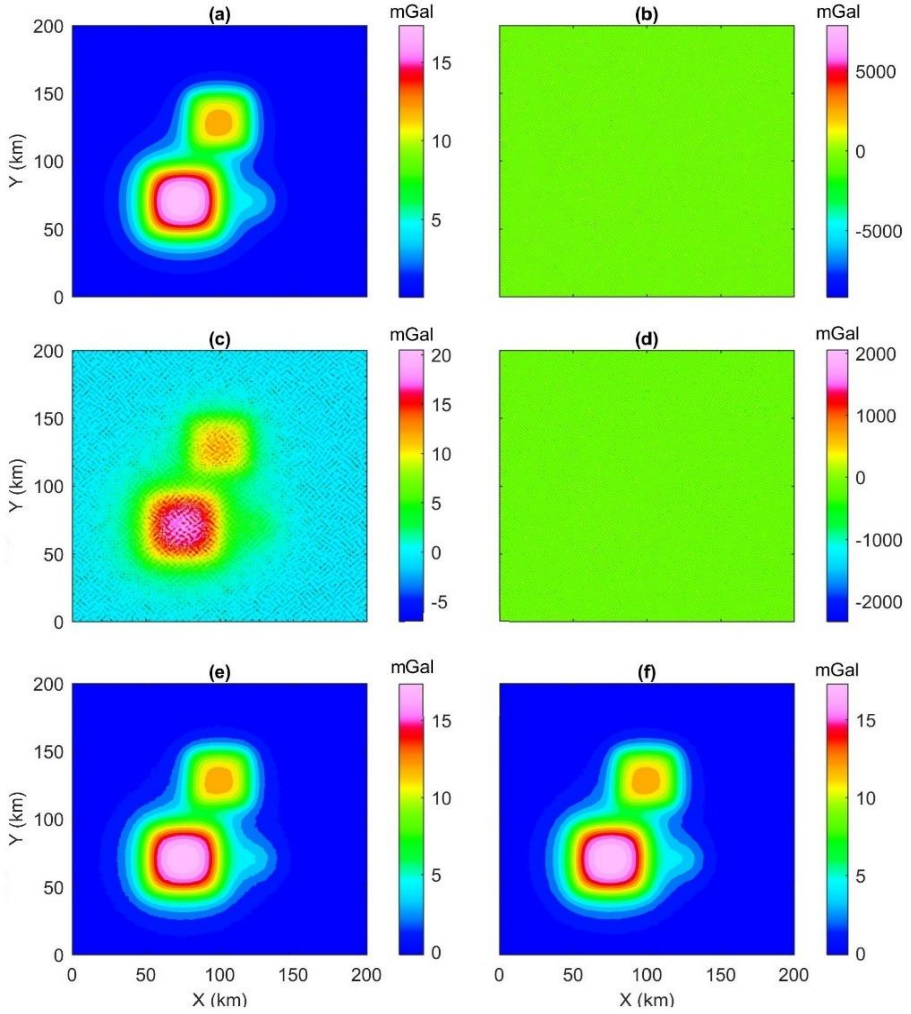

Figure 8. Downward continued field at depth of 5 km (a), 5 km downward continued field of the noisy anomaly using Taylor series with frequency domain derivatives (b), ISVD derivatives (c), FD derivatives (d), T-N derivatives (e), and β-VDR derivatives (f)

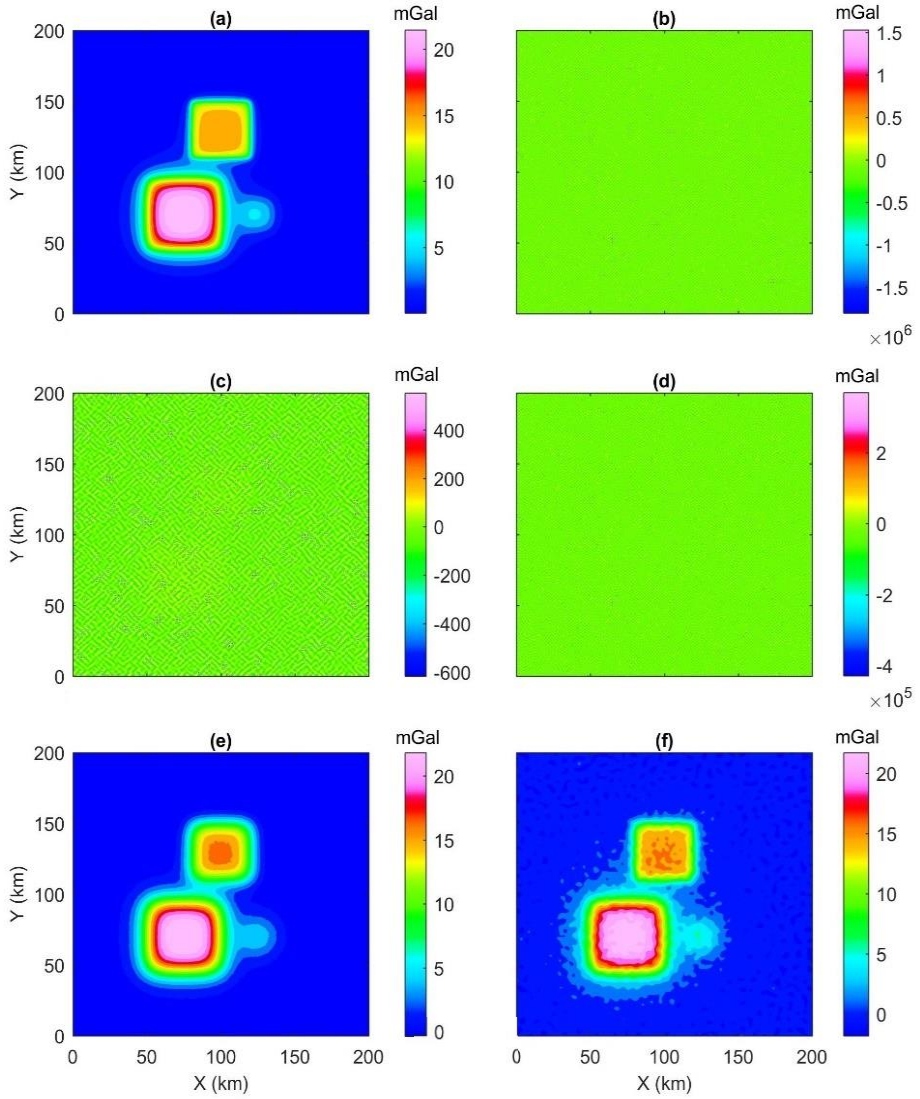

Figure 9. Downward continued field at depth of 10 km (a), 10 km downward continued field of the noisy anomaly using Taylor series with frequency domain derivatives (b), ISVD derivatives (c), FD derivatives (d), T-N derivatives (e), and β-VDR derivatives (f)

Figs. 10a-10c present the EHD obtained from β-VDR derivatives using β = 40, 50, and 60, respectively. These figures show that the results exhibit lower noise levels than those in Fig. 7f. In addition, the results appear more stable as β increases. Figs. 10d-10f present the β-VDR downward continuation fields using β = 40, 50, and 60, respectively. Similar to the EHD results, the β-VDR downward continuation fields are less noisy when β increases. The downward continuation results with β = 50 and 60 show a clear peak over body C, which is not found in the downward continuation fields obtained with the T-N method or the β-VDR method with β = 35.

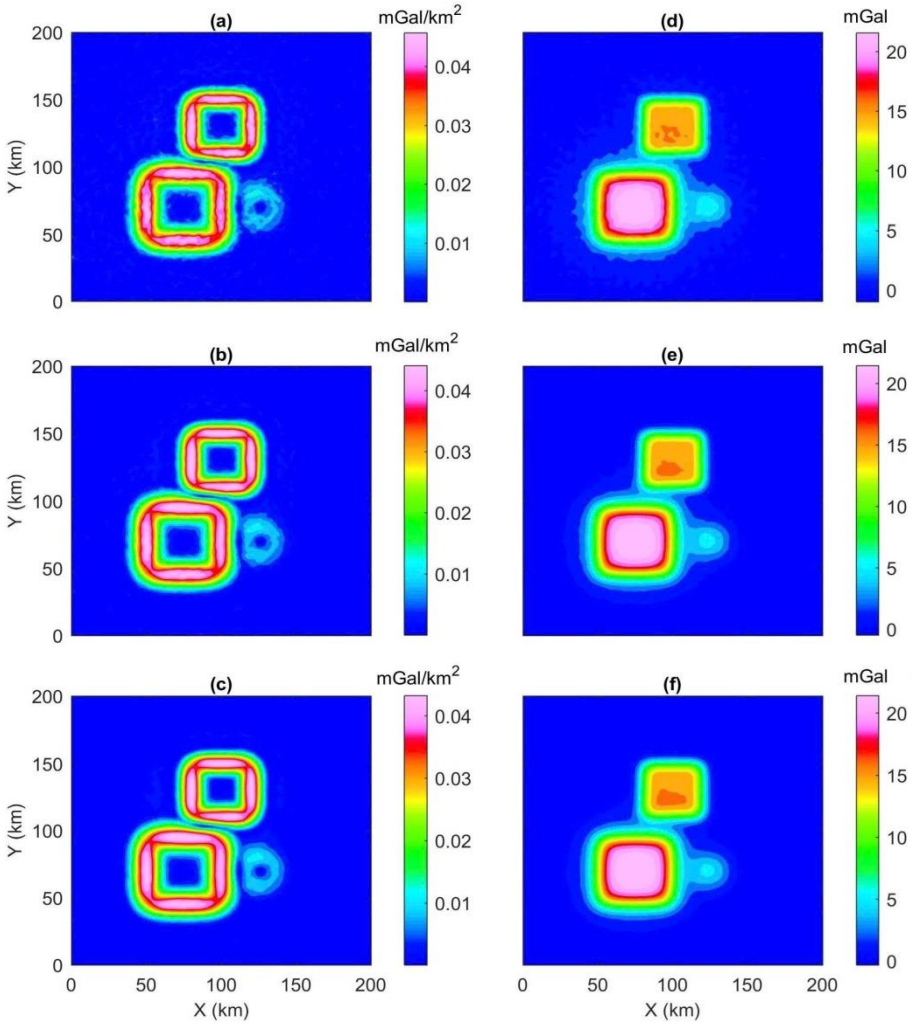

Figure 10. EHD of noisy data by using the β-VDR method with β = 40 (a), 50 (b), and 60 (c); 10 km downward continued field of the noisy anomaly by using the β-VDR method with β = 40 (d), 50 (e), and 60 (f)

4. Real application

Since the β-VDR outperforms other methods overall, we used it to enhance the gravity data of the SW Sub-basin in the East Sea (Fig. 11a). This basin has a V-shaped geometry related to the SW-ward propagation of the spreading center during the opening of the East Sea. Located in the southwest of the East Sea, the SW Sub-basin is characterized by a slow seafloor spreading rate with NE-SW tectonic trends. Gravity data over smaller regions of this basin were previously interpreted and enhanced by Nguyen et al. (2020), Tran and Nguyen (2020), Pham (2025a), among others.

In this study, we used the gravity data from the gravity model developed by Sandwell et al. (2014). This model integrates newly acquired radar altimetry measurements from the CryoSat-2 and Jason-1 satellites, whose advanced altimeter systems provide significantly higher accuracy than earlier missions. When combined with previously available datasets, these observations enabled

the construction of a global marine gravity model with roughly twice the accuracy and a 2–4-fold improvement in gravity-field resolution compared with earlier products. With an accuracy of up to 2 mGal and a grid spacing of 1′ × 1′, Sandwell et al. (2014) demonstrated that their gravity model is highly effective in resolving features such as oceanic spreading centers, fault systems, and seamount features that were not clearly expressed in previous gravity models. To obtain the Bouguer anomaly presented in Fig. 11b, the gravity effect of seawater was replaced with the gravity effect of rock using a density of 2.67 g/cm^3, allowing the resulting anomaly map (Fig. 11b) to reflect better subsurface density variations associated with geological structures.

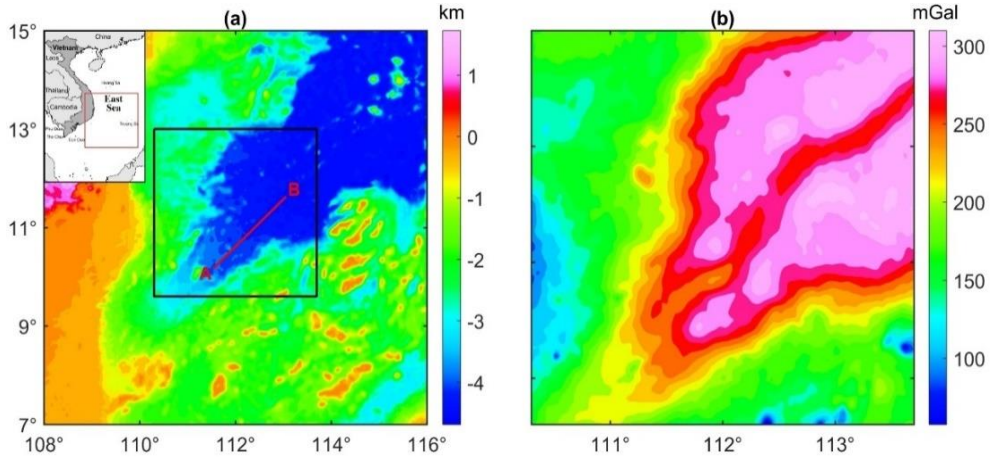

Figure 11. (a) Bathymetric map indicating the location of the SW Sub-basin (black box) and seismic profile (red line), (b) Bouguer anomaly data

Figs. 12a-12c depict the first, second, and third vertical derivatives of the Bouguer data of the SW Sub-basin. The first vertical derivative enhances shallow- and intermediate-depth structures, revealing several elongated anomalies that trend NE–SW primarily. The higher-order derivative further sharpens these features but also amplifies high-frequency signals, making small-scale variations more prominent. The derivatives in Figs. 12a-12c were used to compute the EHD filter with i ranging from 0 to 3 (Fig. 12d). The EHD lineaments and their rose diagram were determined and shown in Fig. 12d. The latter indicates that the EHD filter clearly enhances the NE-SW-trending structures in the basin. Many other geologic boundaries are also defined in the basin using the peaks in the EHD map. Figs. 12e and 12f show downward continuation transformations at depths of 2 and 3 km using the β-VDR derivatives, respectively. Both maps improve the resolution of the Bouguer gravity map. Several anomalies that appear merged in the Bouguer gravity map are effectively separated through the downward continuation (Figs. 12e and 12f). At a greater downward continuation depth (Fig. 12f), small-scale signals and structural patterns become more distinct and are more clearly visible.

For comparison, we extract the EHD profile and the 3 km downward continuation field along the seismic profile shown in Fig. 11a. Fig. 13a illustrates how downward continuation enhances structural information along the seismic profile. In Fig. 13a, the Bouguer anomaly, extended to a depth of 3 km, reveals higher-amplitude, better-defined variations than the original surface anomaly, indicating improved resolution. The EHD peaks in Fig. 13b are related to basement

undulations. When compared with the seismic section in Fig. 13c, the major features labelled A through G show a strong correspondence between downward continuation anomalies and the seismic basement geometry. Elevated basement structures (e.g., A, C, F, and G) align with pronounced peaks in the downward continuation field. At the same time, lower relief zones (e.g., B, D, and E) coincide with weak gravity responses.

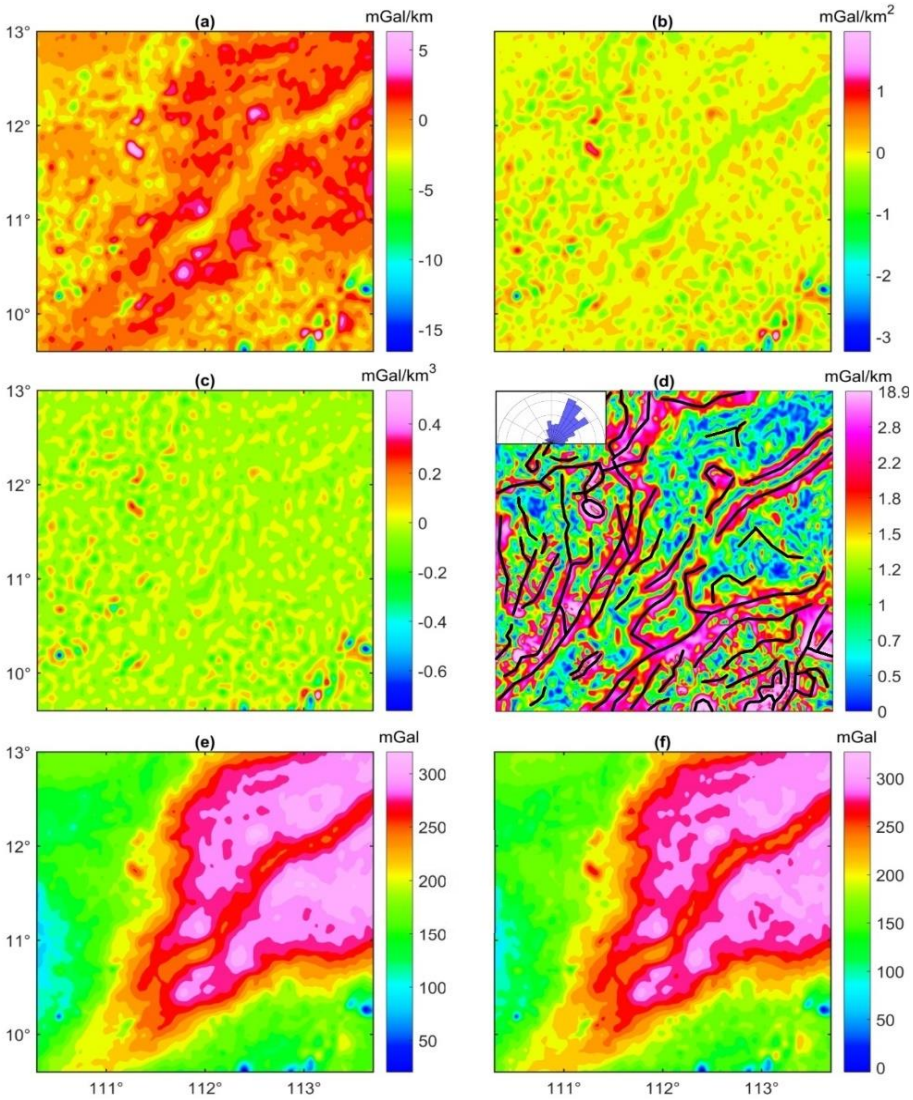

Figure 12. Enhancements of the map in Fig. 11(b): (a) First vertical derivative, (b) Second vertical derivative, (c) Third vertical derivative, (d) EHD, (e) Downward continuation of 2 km, (f) Downward continuation of 3 km. The black lines in (d) show the lineaments extracted from the EHD map, with the rose diagram shown in the inset.

5. Discussions

The standard frequency method for computing derivatives of potential fields is based on the Fourier transformation. However, this transformation can amplify the influence of noise; as a result, the procedure

becomes susceptible to instability caused by data noise (Figs. 2b, 3b, and 4b). In the free-noise case, the standard frequency method also becomes ineffective for calculating high-order derivatives (Figs. 3a and 4a). Since the ISVD method combines the vertical integration filter, known as a smoothing filter, with the finite difference approach, it is more stable than the standard frequency method (Figs. 2d, 3d, and 4d). The FD method uses upward continuation and original surface fields; therefore, it has a lower noise level than the standard frequency method (Figs. 2f, 3f, and 4f). However, this method is more sensitive to noise than other approaches (Figs. 2f, 3f, and 4f). The T-N method combines Taylor series and fields at different heights. This formulation reduces noise more effectively than the frequency-domain and FD approaches (Figs. 2h, 3h, and 4h). Different from the FD and T-N methods, the β-VDR method uses only upward continuation fields. This is why this method allows lower degradation of the signal-to-noise ratio than other approaches, especially when higher-order derivatives are calculated (Figs. 2j, 3j, 4j, and 6m-6o).

Since derivatives obtained from the β-VDR method is more stable than those computed by using other methods. The edge detection result using β-VDR derivatives is less sensitive to noise than the use of other derivatives (Fig. 7). Although the edges of the sources A and B are clearly enhanced by using β-VDR derivatives, the edges of the source C are faint (Fig. 7f). The reason is that the EHD filter is an amplitude-based method that cannot balance anomalies from shallow and deep sources.

The 5 km downward continuation using β-VDR derivatives are also more stable than other approaches (Fig. 8). The downward continuation result improves the horizontal resolution of the data, making the anomalies sharper (Fig. 8f). It is important to note that, for large-depth downward continuation (i.e., 10 km), the T-N method provides a smoother result than the β-VDR downward continuation. However, by using larger values of the β parameter (i.e., β = 50 or 60), β-VDR derivatives are obtained from upward-continuation datasets at higher observed planes, thereby making derivative computation more stable. For this reason, the β-VDR downward continuations have a lower noise level and closely match the true downward continuation (Figs. 10e and 10f). Similar to the downward continuation, the EHD results also show the smoother edges as β increases (Fig. 10a-10c).

The β-VDR method produced stable Bouguer derivatives for the SW Sub-basin (Figs. 12a-12c). These derivatives were used to further enhance the Bouguer data through the EHD filter and downward continuation. The EHD map clearly shows the boundaries of the oceanic crust. The EHD map also demonstrates a dominant NE-SW trend of the SW Sub-basin. This trend shows a strong correlation with the previously recognized faults in the region (Gao et al., 2009). The NE-SW trending edges may be associated with the SW-ward propagation of the spreading center during the opening of the East Sea in the Oligocene–Miocene period. Downward continuation maps highlight the details of the gravity anomalies of the SW Sub-basin (Figs. 12e and 12f). The stability of the downward continuation calculation at a depth of 3 km is also confirmed by seismic data, where the gravity peaks are in good agreement with the elevated basements. (Fig. 13). The details in the downward continuation maps can substantially improve the resolution of subsequent interpretations in the SW Sub-basin.

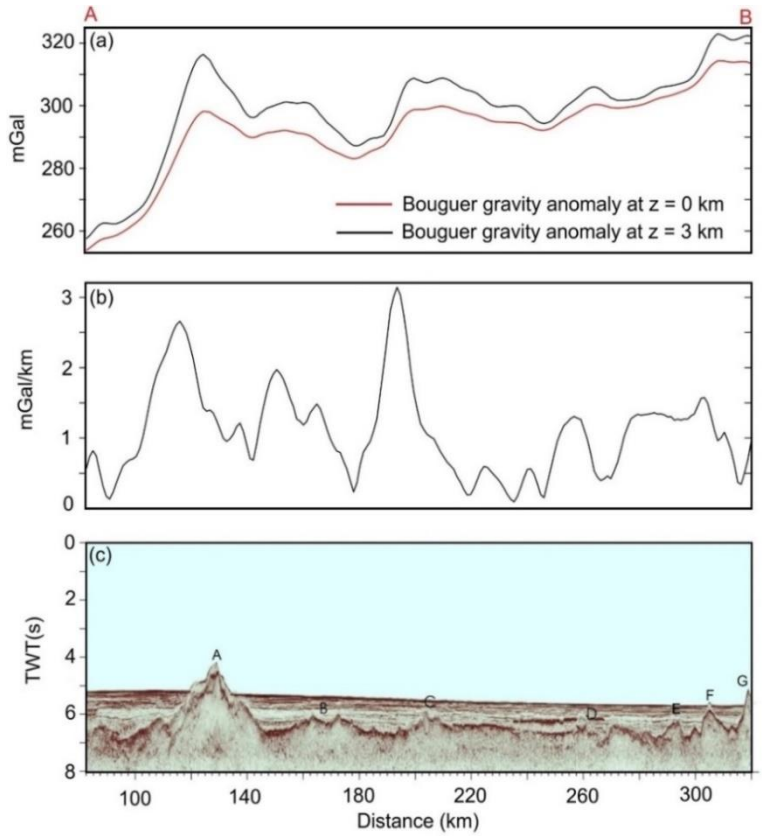

Figure 13. (a) Bouguer anomalies along the profile AB (Fig. 11a) before and after 3 km downward continuation, (b) EHD, (c) Two-way traveltime (TWT) seismic data along the profile AB (Nguyen et al., 2020, Pham, 2025a)

6. Conclusions

This study has evaluated several methods for computing vertical derivatives of potential field data and demonstrated their effects on edge detection and downward continuation. Classical approaches such as the standard frequency and FD methods become increasingly unstable when noise is present or when high-order derivatives are required. The ISVD and T-N methods improve the stability but still amplify noise at higher derivative orders. Among the tested techniques, the The β-VDR method provides the most stable and reliable results, though the β parameter may need to be adjusted depending on the dataset. Because it uses only upward-continued fields, it effectively suppresses high-frequency noise and maintains accuracy for first-, second-, and third-order derivatives. The method also produces the most coherent edge-detection results and the most stable downward-continuation fields, particularly with larger β values. Application to gravity data from the SW Sub-basin further confirms the robustness of β-VDR derivatives. The enhanced maps clearly delineate NE-SW-trending structures and agree well with the seismic basement geometry. The stability of the β-VDR method, even at high derivative orders, makes it especially valuable for applications requiring enhanced resolution, structural mapping, and downward continuation.

Acknowledgements

S.P. Oliveira thanks the support from the National Council for Scientific and Technological Development - CNPq (Brazil), grant number 306516/2024-1.

References

Ai H., Ekinci Y.L., Alvandi A., Deniz Toktay H., Balkaya Ç., Roy A., 2024. Detecting edges of geologic sources from gravity or magnetic anomalies through a novel algorithm based on hyperbolic tangent function. Turk. J. Earth Sci., 33 (6), 684–701. https://doi.org/10.55730/1300-0985.1936.

Ai H., Huang Q., Ekinci Y.L., Alvandi A., Narayan S., 2025. Robust edge detection for structural mapping beneath the Aristarchus Plateau on the Moon using gravity data. Earth and Space Science, 12(8), e2025EA004379. https://doi.org/10.1029/2025EA004379.

Altınoğlu F.F., 2023. Mapping of the Structural Lineaments and Sedimentary Basement Relief Using Gravity Data to Guide Mineral Exploration in the Denizli Basin. Minerals, 13(10), 1276. https://doi.org/10.3390/min13101276.

Alvandi A., Ardestani V.E., Motavalli-Anbaran S.-H., 2024. Novel Detectors Based on the Elliott Function for Mapping Potential Field Data: Application to Aeromagnetic Data from Indiana, United States. Ann. Geoph., 67(6), GP656. https://doi.org/10.4401/ag-9146.

Alvandi A., Ardestani V.E., Motavalli-Anbaran S.-H., 2025. Enhancement of the total horizontal gradient of potential field data using the Modified Gudermannian Function (MGTHG): application to aeromagnetic data from Georgia, USA. Bull. Geophys. Oceanogr., 66(1), 73–94. https://doi.org/10.4430/bgo00479.

Aprina P.U., Santoso D., Alawiyah S., Prasetyo N., Ibrahim K., 2024. Delineating geological structure utilizing integration of remote sensing and gravity data: a study from Halmahera, North Molucca. Indonesia. Vietnam J. Earth Sci., 46(2), 147–168. https://doi.org/10.15625/2615-9783/20010.

Bhattacharyya B.K., 1965. Two-dimensional harmonic analysis as a tool for magnetic interpretation. Geophysics, 30(5), 829–857. https://doi.org/10.1190/1.1439658.

Blakely R.J., 1996. Potential theory in gravity and magnetic applications. Cambridge University Press, Cambridge. ISBN: 0-521-57547-8.

Clarke G.K.C., 1969. Optimum second-derivative and downwardcontinuation filters. Geophysics, 34(3), 424–437. https://doi.org/10.1190/1.1440020.

Cella F., Fedi M., Florio G., 2009. Toward a full multiscale approach to interpret potential fields. Geophys. Prospect., 57(4), 543–557. https://doi.org/10.1111/j.1365-2478.2009.00808.x.

Dean W.C., 1958. Frequency analysis for gravity and magnetic interpretation. Geophysics, 23(1), 97–127. https://doi.org/10.1190/1.1438457.

Eldosouky, A.M., Abd El-Wahed, M.A., Saada, S.A., Attia, M., 2025. New insights into structural and tectonic evolution of Safaga-Semna shear belt, Eastern Desert, Egypt: advanced integration of aeromagnetic, remote sensing and field studies. Geomech. Geophys. Geo-energ. Geo-resour., 11, 31. https://doi.org/10.1007/s40948-025-00946-2.

Evjen H.M., 1936. The place of the vertical gradient in gravitational interpretations. Geophysics, 1(1), 127–136. https://doi.org/10.1190/1.1437067.

Fedi M., Florio G., 2001. Detection of potential fields source boundaries by enhanced horizontal derivative method. Geophys. Prospect., 49(1), 40–58. https://doi.org/10.1046/j.1365-2478.2001.00235.x.

Fedi M., Florio G., 2002. A stable downward continuation by using the ISVD method. Geophys. J. Int., 151(1), 146–156. https://doi.org/10.1046/j.1365-246X.2002.01767.x.

Fedi M., 2002. Multiscale derivative analysis: A new tool to enhance gravity source boundaries at various scales. Geophys. Res. Lett., 29(2), 16-1-16-4. https://doi.org/10.1029/2001GL013866.

Florio G., Fedi M., Pašteka R., 2006. On the application of Euler deconvolution to the analytic signal. Geophysics, 71(6), L87–L93. https://doi.org/10.1190/1.2360204.

Gang Y., Lin Z., 2018. An improved stable downward continuation of potential fields using a truncated Taylor series and regularized vertical derivatives method. J. Geophys. Eng., 15(5), 2001–2008. https://doi.org/10.1088/1742-2140/aac53a.

Gao H., Zhou D., Qiu Y., 2009. Relationship between formation of Zhongyebei basin and spreading of southwest subbasin, East Sea. J. Earth Sci., 20(1), 66–76. Doi: 10.1007/s12583-009-0007-2.

Henderson R.G., 1960. A comprehensive system of automatic computation in magnetic and gravity interpretation. Geophysics, 25(3), 569–585. https://doi.org/10.1190/1.1438736.

Henderson R.G., Zietz I., 1949. The computation of second vertical derivatives of geomagnetic fields. Geophysics, 14(4), 508–516. https://doi.org/10.1190/1.1437558.

Karcol R., Pašteka R., 2025. Regularized derivatives-Revisited. Geophysics, 90(3), G73–G84. https://doi.org/10.1190/geo2023-0787.1.

Luo X., Liu S., Tang X., 2025. A robust method for calculating the vertical derivative of potential fields based on Hilbert transforms. Sci. Rep., 15(1), 18350. https://doi.org/10.1038/s41598-025-99798-9.

Melo F.F., Barbosa V.C.F., 2020. Reliable Euler deconvolution estimates throughout the vertical derivatives of the total-field anomaly. Comput Geosci, 138, 104436. https://doi.org/10.1016/j.cageo.2020.104436.

Melo J.A., Mendonça C.A., Marangoni Y.R., 2023. Python programs to apply regularized derivatives in the magnetic tilt derivative and gradient intensity data processing: A graphical procedure to choose the regularization parameter. Appl. Comput. Geosci., 19, 100129. https://doi.org/10.1016/j.acags.2023.100129.

Miller H.G., Singh V., 1994. Potential field tilt - a new concept for location of potential field sources. J. Appl. Geophys., 32(2–3), 213–217. https://doi.org/10.1016/0926-9851(94)90022-1.

Nabighian M.N., 1972. The analytic signal of two-dimensional magnetic bodies with polygonal cross-section: its properties and use for automated anomaly interpretation. Geophysics, 37(3), 507–517. https://doi.org/10.1190/1.1440276.

Nabighian M.N., 1984. Toward a three-dimensional automatic interpretation of potential field data via generalized Hilbert transforms: Fundamental relations. Geophysics, 49(6), 780–786. https://doi.org/10.1190/1.1441706.

Naidu P., 1966. Extraction of potential field signal from a background of random noise by Strakhov's method. J. Geophys. Res., 71(24), 5987–5995. https://doi.org/10.1029/JZ071i024p05987.

Narayan S., Sahoo S.D., Pal S.K., Kumar U., Pathak V.K., Majumdar T.J., Chouhan A., 2016. Delineation of structural features over a part of the Bay of Bengal using total and balanced horizontal derivative techniques. Geocarto Int., 32(4), 351–366. https://doi.org/10.1080/10106049.2016.1140823.

Narayan S., Kumar U., Pal S.K., Sahoo S.D., 2021. New insights into the structural and tectonic settings of the Bay of Bengal using high-resolution earth gravity model data. Acta Geophys., 69, 2011–2033. https://doi.org/10.1007/s11600-021-00657-8.

Narayan S., Kumar U., Sahoo S.D., Pal S.K., 2024. Appraisal of lineaments patterns and crustal architectures around the Owen fracture zone, Arabian Sea, using global gravity model data. Acta Geophys., 72, 29–48. https://doi.org/10.1007/s11600-023-01170-w.

Nguyen T.N., Van Kha T., Van Nam B., Nguyen H.T.T., 2020. Sedimentary basement structure of the Southwest Sub-basin of the East Vietnam Sea by 3D direct gravity inversion. Mar. Geophys. Res., 41(1), 7. https://doi.org/10.1007/s11001-020-09406-w.

Öksüm E., Altinoglu F.F., Kafadar Ö., 2025. Structural mapping and depth configuration of the Sinanpaşa and western Afyon-Akşehir grabens (SW Türkiye) using advanced gravity data interpretation methods. J. Mt. Sci., 22, 2191–2210. https://doi.org/10.1007/s11629-025-9533-3.

Oliveira S.P., Pham L.T., 2022. A stable finite difference method based on upward continuation to evaluate vertical derivatives of potential field data. Pure Appl. Geophys., 179(12), 4555–4566. https://doi.org/10.1007/s00024-022-03164-z.

Oliveira S.P., Pham L.T., Pašteka R., 2024. Regularization of vertical derivatives of potential field data using Morozov's discrepancy principle. Geophys. Prospect., 72(8), 2880–2892. https://doi.org/10.1111/1365-2478.13534.

Pašteka R., Richter F.P., Karcol R., Brazda K., Hajach M., 2009. Regularized derivatives of potential fields and their role in semi-automated interpretation

methods. Geophys. Prospect., 57(4), 507–516. https://doi.org/10.1111/j.1365-2478.2008.00780.x.

Peters L.J., 1949. The direct approach to magnetic interpretation and its practical application. Geophysics, 14(3), 290–320. https://doi.org/10.1190/1.1437537.

Pham L.T., 2025a. A generalized β-VDR method for computing high-order vertical derivatives: application to downward continuation. Geophys. J. Int., 243(2), ggaf334. https://doi.org/10.1093/gji/ggaf334.

Pham L.T., 2025b. A robust method for computing vertical derivatives of potential fields using upward continuation data. Geophysics, 91(1), G11–G22. https://doi.org/10.1190/GEO-2025-0274.

Pham L.T., Oliveira S.P., Le-Huy M., Nguyen D.V., Nguyen-Dang T.Q., Do T.D., Tran K.V., Nguyen H.-D.-T., Ngo T.-N.-T., Pham H.Q., 2024. Reliable Euler deconvolution solutions of gravity data throughout the β-VDR and THGED methods: application to mineral exploration and geological structural mapping. Vietnam J. Earth Sci., 46(3), 432–448. https://doi.org/10.15625/2615-9783/21009.

Pham L.T., Oliveira S.P., Luu L.D., Do L.T., 2025. Enhancing potential fields using stable downward continuation and boundary filters: application to the Central Highlands, Vietnam. Vietnam J. Earth Sci., 47(2), 236–251. https://doi.org/10.15625/2615-9783/22702.

Reid A.B., Allsop J.M., Granser H., Millett A.J., Somerton I.W., 1990. Magnetic interpretation in three dimensions using Euler deconvolution. Geophysics, 55(1), 80–91. https://doi.org/10.1190/1.1442774.

Reilly W.I., 1969. Interpolation, smoothing, and differentiation of gravity anomalies. New Zealand J. Geol. Geophys., 12(4), 609–627. https://doi.org/10.1080/00288306.1969.10431100.

Roy I.G., 2013. On computing gradients of potential field data in the space domain. J. Geophys. Eng., 10(3), 035007. https://doi.org/10.1088/1742-2132/10/3/035007.

Saada S.A., Eleraki M., Mansour A., Eldosouky A.M., 2025. Insights on the structural framework of the Egyptian Eastern Desert derived from edge detectors of gravity data. Interpretation, 13(1), T71–T85. https://doi.org/10.1190/INT-2024-0023.1.

Sahoo S., Narayan S., Pal S.K., 2022a. Fractal analysis of lineaments using CryoSat-2 and Jason-1 satellite-derived gravity data: Evidence of a uniform tectonic activity over the middle part of the Central Indian Ridge. Phys. Chem. Earth, 128, 103237. https://doi.org/10.1016/j.pce.2022.103237.

Sahoo S., Narayan S., Pal S.K., 2022b. Appraisal of gravity-based lineaments around Central Indian Ridge (CIR) in different geological periods: Evidence of frequent ridge jumps in the southern block of CIR. J. Asian Earth Sci., 239, 105393. https://doi.org/10.1016/j.jseaes.2022.105393.

Sandwell D.T., Müller R.D., Smith W.H.F., Garcia E.S.M., Francis R., 2014. New global marine gravity model from CryoSat-2 and Jason-1 reveals buried tectonic structure. Science, 346(6205), 65–67. https://doi.org/10.1126/science.1258213.

Tatchum C.N., Tabod C.T., Koumetio F., Manguelle-Dicoum E., 2011. A gravity model study for differentiating vertical and dipping geological contacts with application to a Bouguer gravity anomaly over the Foumban shear zone, Cameroon. Geophysica, 47(1–2), 43–55.

Thompson D.T., 1982. EULDPH: A new technique for making computer- assisted depth estimates from magnetic data. Geophysics, 47(1), 31–37. https://doi.org/10.1190/1.1441278.

Tran K.V., Nguyen T.N., 2020. A novel method for computing the vertical gradients of the potential field: application to downward continuation. Geophys. J. Int., 220(2), 1316–1329. https://doi.org/10.1093/gji/ggz524.

Zhang H., Ravat D., Hu X., 2013. An improved and stable downward continuation of potential field data: The truncated Taylor series iterative downward continuation method. Geophysics, 78(5), J75–J86. https://doi.org/10.1190/geo2012-0463.1.